General relativistic moving-mesh hydrodynamics simulations with Arepo and applications to neutron star mergers

Georgios Lioutas[1,2]⋆, Andreas Bauswein[1,3], Theodoros Soultanis[4,5], Rüdiger Pakmor[6], Volker Springel[6], Friedrich K. Röpke[4,7]

[1]GSI Helmholtzzentrum für Schwerionenforschung, Planckstraße 1, 64291 Darmstadt, Germany
[2]Department of Physics and Astronomy, Ruprecht-Karls-Universität Heidelberg, Im Neuenheimer Feld 226, 69120 Heidelberg, Germany
[3]Helmholtz Research Academy Hesse for FAIR (HFHF), GSI Helmholtz Center for Heavy Ion Research, Campus Darmstadt, Germany
[4]Heidelberger Institut für Theoretische Studien, Schloss-Wolfsbrunnenweg 35, 69118, Heidelberg, Germany
[5]Max-Planck-Institut für Astronomie, Königstuhl 17, 69117 Heidelberg, Germany
[6]Max-Planck-Institut für Astrophysik, Karl-Schwarzschild-Str. 1, D-85748, Garching, Germany
[7]Zentrum für Astronomie der Universität Heidelberg, Institut für Theoretische Astrophysik, Philosophenweg 12, D-69120 Heidelberg, Germany

Accepted XXX. Received YYY; in original form ZZZ

ABSTRACT

We implement general relativistic hydrodynamics in the moving-mesh code Arepo. We also couple a solver for the Einstein field equations employing the conformal flatness approximation. The implementation is validated by evolving isolated static neutron stars using a fixed metric or a dynamical spacetime. In both tests the frequencies of the radial oscillation mode match those of independent calculations. We run the first moving-mesh simulation of a neutron star merger. The simulation includes a scheme to adaptively refine or derefine cells and thereby adjusting the local resolution dynamically. The general dynamics are in agreement with independent smoothed particle hydrodynamics and static-mesh simulations of neutron star mergers. Coarsely comparing, we find that dynamical features like the post-merger double-core structure or the quasi-radial oscillation mode persist on longer time scales, likely reflecting a lower numerical diffusivity of our method. Similarly, the post-merger gravitational wave emission shows the same features as observed in simulations with other codes. In particular, the main frequency of the post-merger phase is found to be in good agreement with independent results for the same binary system, while, in comparison, the amplitude of the post-merger gravitational wave signal falls off slower, i.e. the post-merger oscillations are less damped. The successful implementation of general relativistic hydrodynamics in the moving-mesh Arepo code, including a dynamical spacetime evolution, provides a fundamentally new tool to simulate general relativistic problems in astrophysics.

Key words: methods: numerical – hydrodynamics – stars: neutron – neutron star mergers – gravitational waves

1 INTRODUCTION

Numerical simulations are an important tool to study astrophysical systems involving compact objects such as core-collapse supernovae and binary mergers (Janka 2012; Faber & Rasio 2012). The interpretation of the observations and the extraction of physics from such astronomical measurements to a large extent rely on numerical modelling of these events. For instance, observing binary neutron star (BNS) mergers provides the opportunity to study properties of high-density matter and the formation of heavy elements among several other fascinating aspects like short gamma-ray bursts. The recent simultaneous measurement of the inspiral stage of the BNS merger GW170817 and its electromagnetic counterpart, and especially the conclusions drawn from it, highlight the importance of numerical studies of these systems (Abbott et al. 2017a,b; Villar et al. 2017). Simulating compact objects can be challenging because many scenarios require the concurrent resolution of disparate length and time scales of a highly dynamical system in three dimensions and the inclusion of various other physical effects.

The bulk dynamics of such systems is governed by relativistic hydrodynamics in combination with a dynamical spacetime. There exist several approaches to numerically treat relativistic hydrodynamics: most prominent are Eulerian grid-based methods (including finite-difference, finite-volume or discontinuous Galerkin schemes) and Lagrangian smoothed particle hydrodynamics (SPH) (for reviews see e.g. Wilson & Mathews 2003; Font 2008; Alcubierre 2008; Baumgarte & Shapiro 2010; Rezzolla & Zanotti 2013; Rosswog 2015; Martí & Müller 2015; Shibata 2015, and references therein). Font (2008), Baiotti & Rezzolla (2017) and Foucart et al. (2022) provide a survey of codes currently used to tackle general relativistic hydrodynamics (GRHD) problems mostly in the context of binary mergers, and Liptai & Price (2019); Rosswog & Diener (2021) present some recent relativistic SPH tools.

Both Eulerian grid-based methods and SPH have specific advantages and limitations (see the above references for more detailed discussions). Eulerian methods solve the GRHD equations on a static mesh, where many modern codes include (adaptive) mesh refinement

⋆ E-mail: g.lioutas@gsi.de

techniques to resolve specific regions of interest. These methods accurately resolve shocks and fluid instabilities through the implementation of high-resolution shock-capturing methods. However, they may suffer from grid effects, require a special treatment of vacuum regions, and, in the case of compact object mergers, following small amounts of high velocity ejecta at large distances can be challenging.

SPH solves the Lagrangian hydrodynamics equations (comoving with the fluid) on particles representing a certain amount of rest mass. Advection and rest mass conservation are treated with high accuracy and the scheme offers an inherently adaptive resolution. Vacuum regions do not require a special treatment and tracer particles for nucleosynthesis calculations are trivially implemented. Traditionally, SPH is considered to resolve shocks and fluid instabilities poorer compared to high-resolution shock-capturing methods (but see e.g. Rosswog 2015, and references therein for more modern techniques showing significant improvements). Notably, the Einstein equations cannot be solved in a particle-based discretization and thus require the inclusion of an additional computational grid and corresponding communication between both computational structures (similar problems may arise for treating other non-zero fields in the vacuum like magnetic fields).

Springel (2010) introduced the moving-mesh code Arepo, which combines some of the advantages of Lagrangian SPH and Eulerian mesh-based hydrodynamics. Arepo solves Newtonian hydrodynamics with a finite-volume approach on a moving unstructured mesh, which is constructed based on a set of mesh-generating points. The moving-mesh approach retains many of the advantages of mesh-based methods, while the mesh-generating points can move in an arbitrary way (see Springel 2010, for more details). Over the last years, Arepo has been employed for a wide range of astrophysical problems in cosmology, Type Ia supernovae, the common envelope phase in binary stars and various other systems (see e.g. Pakmor et al. 2013; Vogelsberger et al. 2014; Ohlmann et al. 2016; Weinberger et al. 2017; Koudmani et al. 2019; Schneider et al. 2019; Gronow et al. 2021; Pakmor et al. 2022). A number of other moving-mesh codes have subsequently been developed and applied to various astrophysical problems (Duffell & MacFadyen 2011, 2012; Gaburov et al. 2012; Duffell & MacFadyen 2013; Yalinewich et al. 2015; Vandenbroucke & De Rijcke 2016; Chang et al. 2017; Ayache et al. 2022). All these applications have generally shown the usefulness and benefits of the moving-mesh approach as compared to more traditional schemes.

Moving-mesh codes can follow the fluid motion and allow to flexibly place resolution in physically interesting regions. Hence, they offer adaptive resolution, which follows the matter motion including the possibility to split or merge cells and by this to adaptively increase or decrease the resolving power. The quasi-Lagrangian nature of the scheme reduces numerical advection errors. These elements make moving-mesh codes particularly interesting for simulating compact objects and in particular BNS systems. In recent years, some moving-mesh codes have been extended to include GRHD (Ryan & MacFadyen 2017; Chang & Etienne 2020). However, all these implementations currently employ a fixed spacetime, and to date no moving-mesh code evolves the spacetime dynamically, as it would for instance be required to simulate neutron star mergers.

In this work we extend Arepo to simulate general relativistic systems (based on the upgraded implementation described in Pakmor et al. (2016)). We implement GRHD into the code employing the Valencia formulation (Banyuls et al. 1997) and couple to it a solver for a dynamical spacetime. The Einstein equations are solved on an independent overlaid grid adopting the conformal flatness approximation (Isenberg & Nester 1980; Wilson et al. 1996). We also include some additional modules to simulate neutron stars such as a high-density equation of state (EOS). We validate our implementation by computing equilibrium models of isolated neutron stars, which are benchmarked by comparing pulsation frequencies to perturbative results and other codes. Finally, we perform the first moving-mesh simulation of a BNS merger. We evolve the system for almost 40 ms into the post-merger phase and discuss the dynamical properties of the remnant and the characteristics of the GW signal.

The paper is structured as follows. Sec. 2 introduces the theoretical framework of our work. In Sec. 3 we provide details of our numerical implementation focusing on modifications with respect to the original code (Springel 2010; Pakmor et al. 2016). In Sec. 4 we present simulations of isolated, static stars. In Sec. 5 we describe the initial data for BNSs and present a BNS merger simulation. In the last section we provide a summary of our work and outline future plans. Throughout this work we set $c = G = 1$, unless otherwise specified. Greek indices denote spacetime components, while Latin indices refer to spatial components.

2 THEORETICAL FORMULATION

We briefly present the basic equations implemented in the relativistic version of Arepo.

2.1 Field equations

We adopt the ADM formalism (Arnowitt et al. 2008) to foliate the spacetime into a set of non-intersecting spacelike hypersurfaces with a constant coordinate time t. The general metric element then reads

$$ds^2 = g_{\mu\nu}dx^\mu dx^\nu = \left(-\alpha^2 + \beta_i\beta^i\right)dt^2 + 2\beta_i dx^i dt + \gamma_{ij}dx^i dx^j, \quad (1)$$

where $g_{\mu\nu}$ is the spacetime 4−metric, α denotes the lapse function, β^i is the shift vector and γ_{ij} the spatial 3−metric.

In this work we impose the conformal flatness condition (Isenberg & Nester 1980; Wilson et al. 1996), which approximates the spatial part of the metric as

$$\gamma_{ij} = \psi^4\hat{\gamma}_{ij}, \quad (2)$$

where ψ is the conformal factor and $\hat{\gamma}_{ij}$ is the flat metric i.e. $\hat{\gamma}_{ij} = \delta_{ij}$ in Cartesian isotropic coordinates, which we use in our treatment.

Adopting the maximal slicing condition $\mathrm{tr}K_{ij} = 0$, where K_{ij} is the extrinsic curvature, the Einstein equations reduce to a set of five coupled nonlinear elliptic differential equations and read

$$\Delta\psi = -2\pi\psi^5 E - \frac{1}{8}\psi^5 K_{ij}K^{ij}, \quad (3)$$

$$\Delta(\alpha\psi) = 2\pi\alpha\psi^5(E + 2S) + \frac{7}{8}\alpha\psi^5 K_{ij}K^{ij}, \quad (4)$$

$$\Delta\beta^i = -\frac{1}{3}\partial^i\partial_j\beta^j + 2\psi^{10}K^{ij}\partial_j\left(\frac{\alpha}{\psi^6}\right) + 16\pi\alpha\psi^4 S^i, \quad (5)$$

where E, S and S^i are matter sources terms. We adopt the energy-momentum tensor of a perfect fluid, namely

$$T^{\mu\nu} = \rho h u^\mu u^\nu + p g^{\mu\nu}, \quad (6)$$

where ρ is the rest-mass density, $h = 1+\epsilon+p/\rho$ the specific enthalpy, ϵ the specific internal energy, p the pressure and u^μ the 4−velocity of the fluid. Then, in the system of differential Eqs. (3)-(5), the various

matter contributions in the source terms are given by

$$E = \rho h \left(au^0\right)^2 - p, \tag{7}$$

$$S = \rho h \left[\left(au^0\right)^2 - 1\right] + 3p, \tag{8}$$

$$S^i = \rho h \alpha u^0 u^\mu \gamma^i_\mu. \tag{9}$$

Within the conformal flatness approximation, the extrinsic curvature follows directly from the metric elements as

$$K_{ij} = \frac{\psi^4}{2\alpha}\left(\delta_{ik}\partial_j\beta^k + \delta_{jk}\partial_i\beta^k - \frac{2}{3}\delta_{ij}\partial_k\beta^k\right). \tag{10}$$

Following Baumgarte et al. (1998) we introduce the definition $\beta^i = B^i - \frac{1}{4}\partial_i\chi$. Then Eq. (5) can be rewritten as two Poisson-like differential equations for the two auxiliary fields B^i and χ, which read

$$\Delta B^i = 2\psi^{10}K^{ij}\partial_j\left(\frac{\alpha}{\psi^6}\right) + 16\pi\alpha\psi^4 S^i, \tag{11}$$

$$\Delta\chi = \partial_i B^i, \tag{12}$$

and can be solved iteratively.

For more details about the numerical implementation see Sec. 3.7 and Oechslin et al. (2002, 2007).

2.2 General Relativistic Hydrodynamics

The equations of GRHD result from the conservation laws for the energy-momentum tensor $T^{\mu\nu}$ and matter current density $J^\mu = \rho u^\mu$. By choosing a set of appropriate conserved variables, the conservation laws can be written in the form of a first-order flux-conservative hyperbolic system of equations which reads

$$\partial_0\left(\sqrt{\gamma}\boldsymbol{U}\right) + \partial_i\left(\sqrt{\gamma}\boldsymbol{F}^i\right) = \boldsymbol{S}, \tag{13}$$

where $\boldsymbol{U}$ is the state vector, $\boldsymbol{F}^i$ the flux vector, $\boldsymbol{S}$ is the source vector and $\gamma = \det(\gamma_{ij})$ the determinant of the 3-metric (Banyuls et al. 1997; Font 2008).

The state, flux and source vectors are functions of the primitive variables $\boldsymbol{W} = (\rho, v^i, \epsilon)$, where $v^i = (u^i/u^0 + \beta^i)/\alpha$ is the fluid 3−velocity. The state vector consists of the conserved variables and reads

$$\boldsymbol{U} = \begin{pmatrix} D \\ S_i \\ \tau \end{pmatrix} = \begin{pmatrix} \rho W \\ \rho h W^2 v_i \\ \rho h W^2 - p - D \end{pmatrix}, \tag{14}$$

where $W = \alpha u^0 = (1 - \gamma_{ij}v^i v^j)^{-1/2}$ is the Lorentz factor. Furthermore, the flux and source vectors are given by

$$\boldsymbol{F}^i = \alpha \begin{pmatrix} D\left(v^i - \frac{\beta^i}{\alpha}\right) \\ S_j\left(v^i - \frac{\beta^i}{\alpha}\right) + p\delta^i_j \\ \tau\left(v^i - \frac{\beta^i}{\alpha}\right) + pv^i \end{pmatrix}. \tag{15}$$

and

$$\boldsymbol{S} = \alpha\sqrt{\gamma}\begin{pmatrix} 0 \\ T^{\mu\nu}\left(\partial_\mu g_{\nu j} - \Gamma^\lambda_{\nu\mu}g_{\lambda j}\right) \\ \alpha\left(T^{\mu 0}\partial_\mu \ln\alpha - T^{\mu\nu}\Gamma^0_{\nu\mu}\right) \end{pmatrix}, \tag{16}$$

respectively. Here $\Gamma^\lambda_{\nu\mu}$ are the Christoffel symbols of the metric. In the following sections we also employ the definitions $\boldsymbol{\mathcal{U}} = \sqrt{\gamma}\boldsymbol{U}$ and $\boldsymbol{\mathcal{F}}^i = \sqrt{\gamma}\boldsymbol{F}^i$.

2.3 Equation of state

In order to close the system of GRHD Eqs. (13) one needs to specify an EOS. We implement three different options for the EOS.

The first option is an (isentropic) polytropic EOS

$$p = K\rho^\Gamma, \tag{17}$$

$$\epsilon = \frac{K\rho^{\Gamma-1}}{(\Gamma-1)}, \tag{18}$$

where K is the polytropic constant and Γ is the polytropic index.

The polytropic EOS is suitable for an evolution of the system, where the equation for τ is not evolved. The value of the specific internal energy is instead analytically computed based on Eq. (18).

An evolution with the polytropic EOS fails to capture a number of dynamical processes (e.g. shocks). Hence, we implement also an ideal gas EOS

$$p = (\Gamma - 1)\rho\epsilon, \tag{19}$$

which we use for some of our tests (see Sec. 4.1).

Finally, we include a module for hybrid EOSs, which employs a zero-temperature tabulated microphysical EOS complemented by an ideal-gas component to capture thermal effects (Janka et al. 1993). In this EOS, the pressure and specific internal energy read

$$p = p_{\rm cold}(\rho) + p_{\rm th}, \tag{20}$$

$$\epsilon = \epsilon_{\rm cold}(\rho) + \epsilon_{\rm th}, \tag{21}$$

where $p_{\rm cold}$ and $\epsilon_{\rm cold}$ refer to the microphysical EOS and are functions of ρ. The thermal pressure is given by

$$p_{\rm th} = (\Gamma_{\rm th} - 1)\rho\epsilon_{\rm th}, \tag{22}$$

where $\epsilon_{\rm th}$ follows from $\epsilon_{\rm th} = \epsilon - \epsilon_{\rm cold}(\rho)$ and $\Gamma_{\rm th}$ is an appropriately chosen constant, typically in the range between 1.5 and 2 for neutron star applications (Bauswein et al. 2010).

3 NUMERICAL IMPLEMENTATION

We describe the most important steps of our numerical implementation focusing on the modifications and additions to the original Arepo code (Springel 2010; Pakmor et al. 2016). This includes a number of standard methods, as well as additional techniques specific to the moving-mesh approach which we adopt for solving the GRHD equations.

3.1 Time update

Arepo constructs an unstructured Voronoi mesh based on the positions of a set of mesh-generating points. The equations of hydrodynamics are discretized on this mesh in a finite-volume fashion (Springel 2010). Mesh-generating points can be moved simultaneously to the hydrodynamical evolution and this allows a dynamical reconfiguration of the computational grid. For each cell i the volume-integrated conserved variables read

$$\boldsymbol{Q}_i = \int_{V_i} \boldsymbol{\mathcal{U}} dV. \tag{23}$$

The state $\boldsymbol{Q}^n_i$ at time t^n is evolved to the next timestep t^{n+1} using Heun's method, which is a second-order Runge–Kutta scheme

(Pakmor et al. 2016). The time-updated state $\boldsymbol{Q}_i^{n+1}$ is given by

$$\boldsymbol{Q}_i^{n+1} = \boldsymbol{Q}_i^n - \frac{\Delta t}{2}\left(\sum_j A_{ij}^n \hat{\boldsymbol{F}}_{ij}^n(\boldsymbol{W}_{ij}^n, \boldsymbol{W}_{ji}^n) + \sum_j A'_{ij}\hat{\boldsymbol{F}}'_{ij}(\boldsymbol{W}'_{ij}, \boldsymbol{W}'_{ji})\right) + \frac{\Delta t}{2}\left(\boldsymbol{\mathcal{S}}_i^n + \boldsymbol{\mathcal{S}}'_i\right), \tag{24}$$

where the index j runs over all neighbouring cells of cell i and Δt is the timestep. A_{ij} is the interface area between cells i and j, while $\hat{\boldsymbol{F}}_{ij}$ is an approximate Riemann solver estimate for the fluxes through A_{ij} (see Sec. 3.3). The fluxes depend on $\boldsymbol{W}_{ij}$ and $\boldsymbol{W}_{ji}$, which are the reconstructed primitive variables from the center of cell i (or j respectively) to the cell interfaces (see Sec. 3.2). $\boldsymbol{\mathcal{S}}_i = \int_{V_i} \boldsymbol{S} dV$ are the volume-integrated source terms computed for cell i.

Within the Heun method a forward Euler integration has to be performed, which estimates the states at the end of the timestep as

$$\boldsymbol{Q}'_i = \boldsymbol{Q}_i^n - \Delta t \sum_j A_{ij}^n \hat{\boldsymbol{F}}_{ij}^n(\boldsymbol{W}_{ij}^n, \boldsymbol{W}_{ji}^n) + \Delta t \boldsymbol{\mathcal{S}}_i^n. \tag{25}$$

These estimates are used to compute the fluxes $\hat{\boldsymbol{F}}'_{ij}$ and source terms $\boldsymbol{\mathcal{S}}'_i$ at the end of the timestep, where the primitives are recovered and reconstructed from $\boldsymbol{Q}'_i$.

Within the timestep we also move the mesh-generating points and construct a new mesh. As a result, the mesh geometry is different at the beginning and the end of the timestep. This is already apparent in Eq. (24), where we employ different terms for the face areas at the beginning and end of the timestep i.e. A_{ij}^n and A'_{ij} respectively. We update the positions of the mesh-generating points as

$$\boldsymbol{r}_i^{n+1} = \boldsymbol{r}_i^n + \frac{\Delta t}{2}\left(\boldsymbol{w}_i^n + \boldsymbol{w}'_i\right) = \boldsymbol{r}_i^n + \Delta t \boldsymbol{w}_i^n, \tag{26}$$

where $\boldsymbol{r}_i$ denotes the coordinates of the mesh-generating point and $\boldsymbol{w}_i$ is the point's velocity. As described in Pakmor et al. (2016), we keep the velocity of each mesh-generating point constant throughout the whole timestep (i.e. $\boldsymbol{w}'_i = \boldsymbol{w}_i^n$). By doing so, the mesh which is constructed at the end of the current timestep matches the mesh at the beginning of the next timestep (i.e. $A'_{ij} \equiv A_{ij}^{n+1}$). This highlights the benefit of using Heun's method because it requires practically only one mesh construction per timestep.

We update the metric at the beginning of each of the two substeps of Heun's method. We explicitly solve the metric field equations in each Heun substep for the first nine timesteps. Subsequently, we call the metric solver in the first Heun substep of every fifth timestep. For the remaining substeps we estimate the metric using a parabolic extrapolation based on the last three metric solutions. The extrapolation is performed on the metric grid. This approach is accurate as long as the metric fields do not change rapidly, and we find the variations in time to be sufficiently small for the chosen setup. Explicitly solving the metric fields equations in the first timesteps ensures the stability of the scheme after importing initial data and provides the necessary number of collocation points for the extrapolation. We have tested this procedure and find excellent agreement with simulations where we solve the metric equations in every substep. The extrapolation significantly reduces the computational effort.

Arepo can update cell states based on an individual time step for each cell. It employs a power-of-two hierarchy to account for different cell sizes and achieve synchronization (see Springel 2010, for more details). At the moment, we do not employ this functionality and use a single global time step instead. In all the simulations presented in this work we apply the Courant–Friedrichs–Lewy (CFL) condition with a CFL factor $C_{\rm CFL} = 0.3$ to compute the maximum allowed time step Δt_i for each cell. For a cell with volume V_i we employ $[3V_i/(4\pi)]^{1/3}$ as an effective radius for the cell in order to compute Δt_i. Then the global time step is given by

$$\Delta t = \frac{T_{\rm tot}}{2^N}, \tag{27}$$

where $T_{\rm tot}$ is the total simulation time, which is a free parameter, and N is the smallest integer value for which $\Delta t < \min_i \Delta t_i$ holds.

3.2 Reconstruction of primitive variables

To compute the flux terms in Eq. (24), we need to reconstruct the primitive variables from the cell center to the mid-points of the faces. Arepo linearly approximates any quantity ϕ from the center of mass of the cell $\boldsymbol{s_i}$ to any other point within the cell $\boldsymbol{r}$ as

$$\phi(\boldsymbol{r}) = \phi(\boldsymbol{s}_i) + \langle\nabla\phi\rangle_i \cdot (\boldsymbol{r} - \boldsymbol{s}_i), \tag{28}$$

where $\langle\nabla\phi\rangle_i$ is an estimate of the gradient of ϕ within the cell (see Pakmor et al. 2016, for more details on computing the gradient estimate).

Alternatively, we apply the monotonized-central difference (MC) slope limiter (van Leer 1977) to the gradient estimate in order to ensure that the scheme is total variation diminishing (Harten 1983, 1984). We follow the approach outlined in Darwish & Moukalled (2003) for the extension of slope limiters to unstructured grids. Other choices for the slope limiter are also possible. However, the MC slope limiter was shown to perform better in simulations of single relativistic stars (Font et al. 2002).

For the simulations that we present in this work, we employ slope-limited reconstruction. We also highlight that there is ongoing work on higher-order reconstruction schemes on moving meshes (see e.g. Dumbser et al. 2017; Gaburro et al. 2020, and references therein).

3.3 Riemann problem

The original (Newtonian) implementation of Arepo solves the Riemann problem at each face in the rest-frame of the face. This involves estimating the velocity $\tilde{\boldsymbol{w}}_{ij}$ of the common face between each pair of neighbouring cells i and j (see Sec. 3.3 in Springel 2010, for how to estimate $\tilde{\boldsymbol{w}}_{ij}$) and boosting the corresponding cell states by $\tilde{\boldsymbol{w}}_{ij}$. The states on both sides of the mid-point of the face (denoted as left/right) follow from reconstructing the primitive variables. In order to apply an approximate 1D Riemann solver, the left/right states need to be rotated such that the $x-$axis aligns with the normal vector of the face. The solution of the Riemann problem follows from sampling the self-similar solution along $x/t = 0$. The solution is then rotated and boosted back to the initial "lab" frame and used to compute the flux terms in Eq. (24).

In our general relativistic treatment we do not perform the exact same steps. Instead, we follow a different methodology introduced in Duffell & MacFadyen (2011) and solve the Riemann problem in the "lab" frame. In particular, we employ the HLLE solver (Harten et al. 1983; Einfeldt 1988) and sample the solution along $x/t = \tilde{\boldsymbol{w}} \cdot \hat{\eta}$ to capture the correct HLLE state, where $\hat{\eta}$ is the (outward) normal vector to the face. The numerical fluxes, which enter Eq. (24), then read

$$\hat{\boldsymbol{F}}_{ij} = \boldsymbol{\mathcal{F}}_{ij}^{\rm 1D} - \tilde{\boldsymbol{w}}_{ij} \cdot \hat{\eta} \boldsymbol{\mathcal{U}}_{ij}^{\rm 1D}, \tag{29}$$

where $\boldsymbol{\mathcal{F}}_{ij}^{\rm 1D}$ and $\boldsymbol{\mathcal{U}}_{ij}^{\rm 1D}$ are computed by the HLLE solver in the "lab" frame. The second term in Eq. (29) accounts for advection by the moving face.

3.4 Conversion from conserved to primitive variables

It is evident from Eq. (24) that at the end of each timestep we know the volume-integrated conserved variables $\boldsymbol{Q}$, or in turn the conserved variables $\boldsymbol{U}$. To solve the GRHD equations one needs to compute quantities (e.g. the fluxes $\boldsymbol{F}^i$ and sources $\boldsymbol{S}$) which require the primitive variables. While $\boldsymbol{U}$ analytically follows from the primitive variables, obtaining the primitive from the conserved variables requires a numerical solution. The recovery of primitive variables is a common intricate task of GRHD schemes.

We employ a widely used and tested method (see e.g. Rezzolla & Zanotti 2013), which is based on a Newton–Raphson scheme. As a first step, we express the density and specific internal energy as

$$\rho = \frac{D\sqrt{Q^2 - S^2}}{Q}, \tag{30}$$

$$\epsilon = \left(\sqrt{Q^2 - S^2} - \frac{pQ}{\sqrt{Q^2 - S^2}} - D \right) \Big/ D, \tag{31}$$

based on Eqs. (14) and the definitions $S^2 = \gamma^{ij} S_i S_j$ and $Q = \tau + p + D$. Then, for a generic EOS $p = p(\rho, \epsilon)$, we employ a Newton–Raphson method to solve the equation

$$p - \hat{p}\left[\rho\left(\boldsymbol{U}, p\right), \epsilon\left(\boldsymbol{U}, p\right)\right] = 0, \tag{32}$$

starting from an initial guess for the pressure p (e.g. the pressure at the cell center in the previous timestep for accelerated root-finding). We compute the necessary derivatives $\partial\hat{p}/\partial\rho$ and $\partial\hat{p}/\partial\epsilon$ numerically. As an additional measure we reset the primitive variables to atmosphere values if for a cell $p < 0$ or the density ρ is below a threshold value $\rho_{\rm thr}$ (see Sec. 3.6 for details). The conserved variables are then recomputed for the new primitives.

3.5 Mesh geometry

Arguably two of the most important aspects in a moving-mesh simulation are the initial positions of the mesh-generating points and how the points move during the simulation. The initial distribution of the points determines the initial geometry of the mesh, while point motion determines how the mesh geometry evolves. A mesh which is well-adapted to the geometrical and physical aspects of the problem at hand captures the physics more accurately even with fewer cells, since resolution is distributed more appropriately in the simulation domain.

In the various tests that we present in the following sections, we use different initial mesh-generating point distributions for different tests. Furthermore, we perform both moving-mesh, as well as static-mesh simulations, i.e. calculations where the cells move or remain fixed at their initial positions, respectively. In our moving-mesh simulations each point moves with the local fluid coordinate velocity with possibly a small correction to this velocity to ensure that the mesh does not become too irregular (see Sec. 4 in Springel 2010, for more details). For the mesh regularity we adopt a more recent criterion proposed in Vogelsberger et al. (2012) (see Weinberger et al. 2020, for a summary).

Distributing the mesh-generating points carefully and allowing them to follow the fluid motion ensures that resolution is focused on the physically interesting regions and minimizes advection across cells. However, some problems might additionally benefit from increasing or decreasing the resolution locally in a flexible way. Arepo allows for cell refinement or derefinement based on nearly arbitrary criteria (see Sec. 6 in Springel 2010). Different criteria can be employed to dynamically change the local geometry of the mesh, effectively adding resolution where it is needed and reducing the resolution where it is deemed redundant.

We provide details regarding the initial mesh geometry and whether we enable cell refinement/derefinement in the discussion of each test, since the choices strongly depend on the concrete application. We emphasize that a direct comparison between moving-mesh and static-mesh simulations is not necessarily straightforward, even in cases where the initial meshes are identical in moving-mesh and static-mesh simulations. The reason is that in moving-mesh calculations the cells rearrange over time. Hence the mesh can in principle evolve to a setup which differs significantly from the initial geometry.

3.6 Additional code details

Grid-based hydrodynamics approaches require a special treatment for vacuum regions. We employ an artificial atmosphere, i.e. we place cells with a very low density $\rho_{\rm atm}$ in vacuum regions. During the evolution the numerical treatment resets the density to this value if the density of a cell falls below a threshold value $\rho_{\rm thr}$. In the tests which we present in the following sections we set $\rho_{\rm thr} = 10 \times \rho_{\rm atm}$ and $\rho_{\rm atm} = (10^{-7} - 10^{-8}) \times \rho_{\rm max}$, where $\rho_{\rm max}$ is the maximum density throughout the whole domain at a given time. This criterion captures cells outside the neutron stars, where one should formally have vacuum. In these cells we also set the velocities to zero, while the pressure and specific internal energy follow from a polytropic EOS with $K = 100$ and $\Gamma = 2$. Subsequently, we update the conserved variables in these atmospheric cells based on the new set of primitives.

Formally, we adopt periodic boundary conditions in our calculations. This choice does not affect the evolution of the system because the outer boundaries are placed far away from the regions of physical interest, where all the cells have densities below the atmosphere threshold. The size of the numerical domain varies in different tests to cover the whole physical system. The exact size does not play an important role as in typical simulations the physical domain of interest is surrounded by atmosphere cells, which can be placed very sparsely further out and thus hardly influence the computational demands.

3.7 Solution of field equations

We solve the metric field Eqs. (3), (4), (11) and (12) on an independent uniform Cartesian grid. We employ a multigrid algorithm (see e.g. Briggs et al. 2000) and solve the differential equations iteratively until they converge. Boundary conditions for the solution of Eqs. (3) and (4) are computed based on a multipole expansion of the fields up to quadrupole order. We impose fall-off boundary conditions in order to solve Eqs. (11) and (12). The metric solver implementation originates from Oechslin et al. (2002), where they provide more details. The grid size is chosen such that it covers the physical domain of interest well.

In our implementation hydrodynamic quantities and metric potentials are solved on different grids. To solve the GRHD equations we need to interpolate the metric fields to various positions e.g. the mesh-generating point positions, the center of mass of Voronoi cells or the mid-point of the interfaces between neighbouring cells. Vice versa, solving the metric field equations requires knowledge of the hydrodynamic variables at the positions of the metric grid points. We perform the mappings in the following way:

(i) *Metric grid to hydro mesh*: Knowing the metric fields on a uniform Cartesian grid, we interpolate to any point if it lies within the metric grid. We interpolate the metric fields with a 3$^{\rm rd}$ order Lagrange

polynomial. We cannot apply the same approach to compute the metric fields at points outside the metric grid domain. Instead, we employ the multipole expansions and fall-off conditions that we used to compute the metric boundary conditions for these distant cells.

(ii) *Hydro mesh to metric grid*: The inverse mapping is significantly more complicated because the hydrodynamics mesh is unstructured. The main component is a tree walk (Springel 2010) to locate the mesh-generating point which lies closest to each metric grid point. At the end of the tree search, each metric grid point is placed in a hydrodynamics cell. We then directly adopt all necessary hydrodynamical variables from the moving-mesh cell for the respective metric grid point.

We have found this simple approach to be rather robust and accurate. As expected, its accuracy improves as the number of hydrodynamic cells increases[1]. Furthermore, it benefits from the fact that physically important regions are more densely populated with mesh points. As a result, the distance between the centers of the moving-mesh cells and the metric grid cells is typically quite small. We plan to further examine this point in the future. Simple extensions (e.g. via the use of gradients $\langle \nabla \phi \rangle$ discussed in Section 3.2) can potentially prove more accurate without significantly adding to the computational cost.

3.8 Gravitational wave backreaction and extraction

The conformal flatness approximation does not include gravitational radiation by construction which, however, can be important in some applications like for instance BNSs. Therefore, we complement our approach by adding a backreaction scheme to emulate gravitational wave energy and angular momentum losses.

We closely follow the implementation of Oechslin et al. (2007), which consists of adding a small, non-conformally flat correction to the metric based on a post-Newtonian analysis presented in Faye & Schäfer (2003) (see also Blanchet et al. 1990). For neutron star merger simulations this approach shows generally a good agreement with fully general relativistic simulations comparing for instance the post-merger gravitational wave emission, black-hole formation or ejecta and torus masses (see e.g. Bauswein et al. 2012, 2013, 2021; Kölsch et al. 2021).

4 TOLMAN-OPPENHEIMER-VOLKOFF STAR

We evolve a static equilibrium neutron star and extract its fundamental radial mode frequency to verify our implementation. For a first test, we evolve a neutron star described by a polytrope while keeping the metric fixed (Cowling approximation). This analysis targets our general relativistic hydrodynamics implementation alone. As a second test, we evolve a neutron star described by a microphysical EOS, while dynamically evolving the spacetime as well. This setup tests our GRHD implementation, our metric solver and their coupling, as well as our microphysics modules.

Table 1 summarizes the features and parameters of all simulations discussed in this paper including the BNS merger run described in Sec. 5.

[1] We for instance compare the baryonic mass on the different grids for the simulations discussed in this work and find that they agree to at least 0.1%. The mass on the metric grid oscillates by this magnitude around the value of the unstructured hydro mesh without any systematic trend.

4.1 Cowling approximation

4.1.1 Initial data

We solve the Tolman-Oppenheimer-Volkoff (TOV) equations and compute a 1.4 $M_\odot$ polytropic neutron star with $K = 100$ and $\Gamma = 2$ (central density $\rho_c = 1.28 \times 10^{-3}$ in $c = G = 1$ units). This stellar model is a common choice and allows us to compare our evolutions within the Cowling approximation with results from previous works (Font et al. 2002).

We map the primitive quantities from the 1D TOV solution to a mesh-generating point distribution which is used to construct a Voronoi mesh. In this simulation the hydrodynamical simulation domain is a cube with side length 58 $M_\odot \approx 85.6$ km, hence significantly larger than the stellar radius ($R \approx 12$km in isotropic coordinates). We set up the mesh-generating points to obtain a uniform Cartesian grid with high resolution in the center of the computational domain to cover the star. This particular mesh setup allows us to compare directly to Font et al. (2002), where also a Cartesian grid is employed. The central, high-resolution mesh is a cube with side length 24 $M_\odot \approx 35.4$ km and a cell size $h = 0.1\ M_\odot \approx 147.6$m. We cover the rest of the simulation domain with points which lead to a low resolution mesh. Throughout the whole evolution these outer parts of the computational domain are atmosphere cells and thus the exact point distribution is irrelevant, provided the mesh-construction algorithm can create a mesh. Even a very low number of mesh-generating points is already sufficient.

We excite the radial mode by adding a radial 3-velocity perturbation of the form

$$\delta v_r = A \sin\left(\frac{\pi r}{R}\right), \tag{33}$$

where $A = -0.005$, r is the radial distance from the stellar center and R is the stellar radius (see e.g. Dimmelmeier et al. 2006).

In our Cowling tests we compute the metric fields at any point in our simulation domain (e.g. mesh-generating point positions, centers of mass of the hydrodynamic cells) by interpolating the high-resolution metric function profiles which we obtain from our TOV solution. We set the atmosphere density to $\rho_{atm} = 10^{-8} \times \rho_{max}$ and consider any cell with $\rho < 10 \times \rho_{atm}$ to be part of the atmosphere. We evolve the polytropic initial data with an ideal gas EOS and thus also evolve the energy equation.

4.1.2 Simulations

Figure 1 shows the evolution of the maximum density normalized to its initial value. The blue line refers to a moving-mesh simulation, while the orange line to a static-mesh run where the mesh-generating points do not move. We notice that they both preserve the initial TOV solution without any significant density drift during the roughly 10ms evolution. We extract the main radial pulsation frequency by a Fourier transform of the density oscillations. We obtain 2.672 kHz for the moving mesh and 2.682 kHz for the static mesh, which are both in excellent agreement with previous results (2.696 kHz in Font et al. 2002). A number of overtones are excited as well. In particular, in the moving-mesh simulation we identify 6 overtones, which all agree within less than 2% with the values reported in Font et al. (2002).

The moving-mesh and static-mesh evolutions are rather similar for the first few milliseconds. However, at later times the moving-mesh setup exhibits some damping in contrast to the static-mesh. This possibly originates from the surface layers. Initially the star contracts while atmosphere cells do not move. This results in a small gap between stellar material and atmosphere, and thus the resolution at

Table 1. Summary of the simulations presented in this study. The first column specifies the type of system simulated. Second column denotes if the spacetime was fixed or evolved dynamically. Third column indicates if the mesh was moving during the simulation. The fourth column contains information about the symmetry of the initial grids, which we employ in the different simulations. Fifth column indicates whether we employ cell refinement and derefinement in the respective simulation. In the sixth column we provide an estimate for the resolution. In moving-mesh simulations the resolution changes dynamically (see main text for more details on each simulation). In the case of the BNS system the resolution refers to the high-density regime in the post-merger phase. Columns seven and eight list the EOS and masses of the systems. Finally, the last column reports the characteristic frequency extracted in every simulation. In the case of TOV stars this refers to the frequency of the radial mode (f_0), while for the BNS system it is the dominant frequency in the post-merger phase. Eighth row provides the perturbative result of the isolated TOV star for comparison.

System	Spacetime	Mesh motion	Hydro grid setup (region around stars)	Cell refinement/ derefinement	Resolution [m]	EOS	Gravitational Mass [$M_\odot$]	Characteristic Frequency
TOV star	Fixed	Moving	Uniform Cartesian	No	≈ 147.6	Ideal gas	1.4	$f_0 = 2.672$ kHz
TOV star	Fixed	Static	Uniform Cartesian	No	≈ 147.6	Ideal gas	1.4	$f_0 = 2.682$ kHz
TOV star	Dynamical	Moving	Spherical	No	≈ 253.7	H4 + $\Gamma_{\rm th} = 1.75$	1.41	$f_0 = 2.318$ kHz
TOV star	Dynamical	Moving	Spherical	No	≈ 191	H4 + $\Gamma_{\rm th} = 1.75$	1.41	$f_0 = 2.343$ kHz
TOV star	Dynamical	Moving	Spherical + Random	No	≈ 191	H4 + $\Gamma_{\rm th} = 1.75$	1.41	$f_0 = 2.349$ kHz
TOV star	Dynamical	Moving	Spherical	No	≈ 162.4	H4 + $\Gamma_{\rm th} = 1.75$	1.41	$f_0 = 2.352$ kHz
TOV star	Dynamical	Static	Spherical	No	≈ 191	H4 + $\Gamma_{\rm th} = 1.75$	1.41	$f_0 = 2.358$ kHz
TOV star	Dynamical	–	Perturbative	–	–	H4	1.41	$f_0 = 2.385$ kHz
BNS merger	Dynamical	Moving	Spherical (based on mass distribution)	Yes	≈ 162	DD2 + $\Gamma_{\rm th} = 1.75$	1.35+1.35	$f_{\rm peak} = 2.56$ kHz

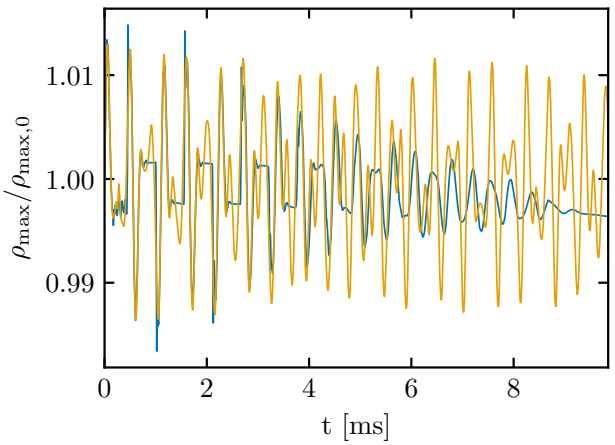

Figure 1. Evolution of the maximum rest-mass density normalized to its initial value for a 1.4 $M_\odot$ TOV neutron star modelled as a polytrope with $K = 100$ and $\Gamma = 2$. The blue line refers to a moving-mesh setup, while the orange line to a static-mesh setup. Both simulations adopt the Cowling approximation. In both cases, a radial velocity perturbation with amplitude -0.005 was applied. See the main text for details regarding the mesh setup.

the stellar surface effectively drops. When the star expands, the stellar surface moves into the atmosphere. During expansion and contraction phases of the star, cells can cross the atmosphere threshold. Cells belonging to the star can become atmosphere, and atmosphere cells can accumulate material to become "active" stellar cells. Overall this leads to a decrease in the resolution close to the surface already after the first few ms. In particular, the static-mesh and moving-mesh simulations have similar resolutions in the interior of the neutron star up to a few hundreds of meters beneath the surface. In the outer meters of the crust, the moving-mesh simulation has a lower resolution, which is probably the main reason for the higher damping. Finally, in the moving-mesh simulation a thin high-resolution shell forms right at the surface because of cells which originally belonged to either the star or the atmosphere.

The cell rearrangement in the moving-mesh evolution highlights that a direct comparison between a static-mesh and a moving-mesh simulation is not necessarily straightforward. Even if the initial mesh geometries match, the moving mesh quickly rearranges and does not have a single resolution that one can compare to the fixed mesh. Furthermore, Cartesian mesh geometries are not an optimal initial mesh setup for simulations of TOV stars because they do not take into account the spherical symmetry of the system. In addition, allowing the cells to move without taking the mass distribution of the system into account can lead to issues close to the surface as reported. The rearrangement of cells close to the surface can create small cells. If these cells are not derefined, which we do not do in our TOV simulations, they can in principle reduce the (global) timestep, hence increasing the required computational effort. We note that the mesh-generation algorithm typically requires more time to construct a Cartesian grid compared to other distributions with the same number of mesh-generating points due to the extra cost required to resolve geometric degeneracies during mesh construction.

4.2 Dynamical spacetime

4.2.1 Initial data

We construct TOV data for a 1.41 $M_\odot$ neutron star configuration (central density $\rho_c = 9.545\times10^{-4}$) described by the H4 EOS (Lackey et al. 2006) modelled as a piecewise polytrope (Read et al. 2009). We complement H4 with a $\Gamma_{\rm th} = 1.75$ thermal ideal-gas component.

The initial mesh-generating point distribution and subsequently the mesh geometry is different from our Cowling tests. We map the 1D TOV data to a spherical distribution of cells located at the center of the simulation domain. We use a total of 85 shells extending up to a distance of 11 $M_\odot \approx 16.2$ km, with an equidistant radial separation $\approx$ 191 m between consecutive shells. In addition to these shells we place a coarse Cartesian grid to fill the rest of the computational domain. This setup is our standard resolution run. In addition, we construct two similar setups with 100 shells (i.e. a resolution of ≈ 162.4 m) and 64 shells (namely a resolution of ≈ 253.7 m), which we employ for higher and lower resolution (moving-mesh) simulations respectively. Finally, we also test a mesh which is similar to our standard resolution,

but we randomly place the mesh-generating points on each shell to eliminate possible grid orientation effects.

In this section we compare the radial mode frequency from our simulations to a calculation with an independent linear perturbation code, which we developed following the approach outlined in Gondek et al. (1997). Unlike Sec. 4.1, we do not compare to results from an independent Cartesian hydrodynamics code. Since the perturbative result is practically exact and the comparison does not rely on choosing the same grid setup, we explore in these tests other choices for the (initial) mesh. We employ a grid that better captures the geometry of the physical system.

In contrast to the previous test, the spacetime evolves dynamically. We solve the metric field equations on a uniform Cartesian grid with 129^3 points with a resolution $h_{\rm M} = 0.3\ M_\odot$. Similar to the Cowling tests, we excite the radial oscillation with a perturbation of the form (33) with $A = -0.001$ and we set $\rho_{\rm atm} = 10^{-8} \times \rho_{\rm max}$ and $\rho_{\rm thr} = 10 \times \rho_{\rm atm}$.

4.2.2 Simulations

In Fig. 2 we present the time evolution of the normalized maximum density of the 1.41 $M_\odot$ H4 stellar model with a moving mesh (blue) and a static mesh (orange) with our standard resolution setup. Again, we compute the fundamental radial pulsation frequency. Using a Fourier transform of the density oscillations we obtain 2.343 kHz for the moving mesh and 2.358 kHz for the static mesh. For comparison, the perturbative calculation gives 2.385 kHz. Deviations of the order of one per cent are comparable to what is found by other codes e.g. (Font et al. 2002).

Moving-mesh runs with the higher and lower resolution setups result in frequencies of 2.352 kHz and 2.318 kHz respectively, i.e. the frequencies approach the perturbative result with increasing resolution. In addition, we perform a moving-mesh simulation with a initial mesh setup with standard resolution ($\approx$ 191 m) including a random component to slightly offset the mesh-generating points. We obtain 2.349 kHz, which is slightly higher than the result from the same resolution setup without the random component. We note that including the random component in the mesh setup reduces grid effects, while only slightly increases the damping in the maximum density oscillation. The overall agreement in the frequencies validates our implementation of GRHD and the metric solver, as well as their coupling in a realistic setup which employs a microphysical EOS.

The moving-mesh and static-mesh standard resolution simulations of the star preserve the initial TOV solution during the whole simulation time with no significant drift in the central density. The oscillation in the moving-mesh simulation show some damping over time, but the amplitude is still sizable at the end of the calculation. This is not surprising because in moving-mesh simulations of stationary problems secular drifts of the mesh-generating points occur, in particular close to the surface, and lead to an irregular mesh configuration. In principle, specific implementations such as modifying the cell motion close to the surface and suppressing small drifts are likely to improve the behavior in quasi-stationary situations. Since our work is targeted to highly dynamical problems, where we do not face the same issues, we do not follow up on these points here.

5 BINARY NEUTRON STAR MERGERS

In this section we discuss a BNS merger simulation. This is the first simulation of a neutron star merger using a moving mesh and we show that this approach can be successfully used to simulate such systems.

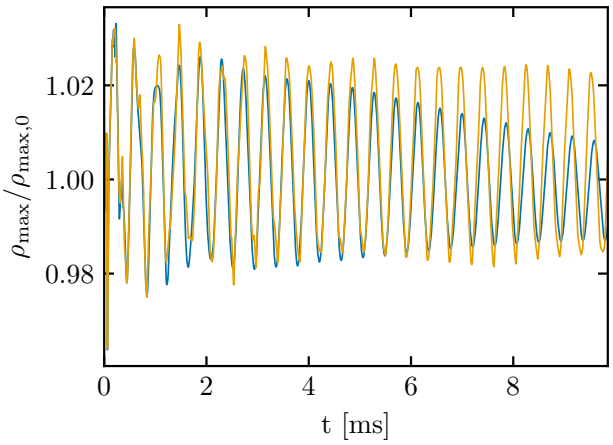

Figure 2. Normalized maximum rest-mass density from a moving-mesh (blue line) and a static-mesh (orange line) evolution of a 1.41 $M_\odot$ star described by the H4 EOS. The spacetime is evolved dynamically and the metric field equations are solved on a grid with 129^3 points and resolution 0.3 $M_\odot$. The pulsation is excited with a radial velocity perturbation with amplitude −0.001. See the main text for a description of the initial mesh geometry.

5.1 Initial data and setup

We employ the DD2 EOS (Hempel & Schaffner-Bielich 2010; Typel et al. 2010) as a zero-temperature β-equilibrium tabulated microphysical EOS. We remark that the DD2 model provides the full temperature and composition dependence of the EOS. In this work however, for convenience, we only use a slice at $T = 0.1$ MeV as the lowest temperature provided by the EOS table. We supplement the barotropic EOS with a thermal ideal-gas component with $\Gamma_{\rm th} = 1.75$, as described in Sec. 2.3 (see Bauswein et al. 2010, for more details). DD2 is marginally compatible with current observational constraints on the tidal deformability from GW170817 (Abbott et al. 2017a, 2019) and fully consistent with mass measurements of various binary systems (Demorest et al. 2010; Antoniadis et al. 2013; Arzoumanian et al. 2018; Linares et al. 2018; Cromartie et al. 2020).

We construct initial data for an equal-mass BNS system in a circular quasi-equilibrium orbit using LORENE[2] (Gourgoulhon et al. 2001). The two companion neutron stars have a gravitational mass of $M = 1.35\ M_\odot$ (at infinite binary separation) and are irrotational. The initial separation is 26 $M_\odot \approx 38.4$ km. LORENE solves the metric field equations using the conformal flatness approximation like our code. As a result, we do not observe an unphysical transient at the beginning of our simulation as compared to fully relativistic simulations, which react to the missing GW content of the initial data. Hence, we can start our simulation from a relatively small initial separation of the two companion stars.

We map the initial data to a distribution of points which follows approximately the mass distribution. In particular, around each star, we construct spherical shells and then distribute cells on each shell based on the HEALPix algorithm by Górski et al. (2005). The grid setup is described in detail in Ohlmann et al. (2017). The radial

[2] http://www.lorene.obspm.fr/

positions of the shells are determined based on the density profile of a TOV solution with $M = 1.35\ M_\odot$, which we modify in the outer parts of the star. Between the distances $r_{\rm in} = r(\rho_c/2)$ and $r_{\rm out} = 1.1 \times R$ we set $\rho\sqrt{\gamma} = \rho\psi^6$ to its value at $r_{\rm in}$. Here ρ_c is the central density and R the radius of the TOV star. This grid thus extends beyond the stellar radius. This particular setup guarantees that the resolution does not drop abruptly close to the surface because of the steep density gradient. Moreover, we resolve the regions around R, which is important because the stars in the binary are not perfect spheres, but deformed. In principle this construction leads to a mesh with no grid orientation effects (see Ohlmann et al. 2017, for more details). We cover (vacuum) regions outside the spheres with radius $r_{\rm out}$ around each star with a coarse uniform Cartesian mesh with resolution $10.1\ M_\odot$. The atmosphere density is set to $\rho_{\rm atm} = 10^{-7} \times \rho_{\rm max}$ and $\rho_{\rm thr} = 10 \times \rho_{\rm atm}$. We do not impose any symmetries during the simulation. The metric field equations are solved on a uniform Cartesian grid with 129^3 points and resolution $0.8\ M_\odot$.

During the simulation we allow for cell refinement and derefinement. We set a cell target mass $m_{\rm cell,0} = 1.68 \times 10^{-6}\ M_\odot$, which is the same that we used to find the radial positions of cells in the mesh-constructing algorithm (see Ohlmann et al. 2017, for more details). We refine cells with mass $m_{\rm cell} > 2 \times m_{\rm cell,0}$ and derefine cells with mass $m_{\rm cell} < m_{\rm cell,0}/2$. Furthermore, for each cell we check the volume of every neighbouring cell. We ensure that a cell is not derefined if $V > 1.5 \times V^{\rm min}_{\rm ngb}$, where V the cell volume and $V^{\rm min}_{\rm ngb}$ the volume of the smallest neighbouring cell. We refine any cell for which $V > 5 \times V^{\rm min}_{\rm ngb}$ holds. To avoid creating an irregular mesh through the refinement process, in all cases we do not refine highly distorted cells i.e. cells with $\alpha_{\rm max} \geq 3.375$, where $\alpha_{\rm max} = \max_i \left(\sqrt{A_i/\pi}/h_i\right)$ is used to estimate how round a cell is based on the area of each face A_i and its distance from the mesh-generating point h_i (see Vogelsberger et al. 2012, for more details). This combination of criteria guarantees that we have a mesh where many cells have comparable mass content, while we also resolve the surface with decent resolution. Roughly 1.7×10^6 cells with $\rho > \rho_{\rm thr}$ resolve physically interesting regions. Notably, shortly after the beginning of the simulation, we find only a small number of cells outside the two stars due to cell derefinement. Hence, in our approach the hydrodynamical domain can be arbitrarily large with practically no effect on the computational time.

We compare the maximum density (see Fig. 3) and lapse function evolution during the first few milliseconds of our binary system evolution to an independent simulation of a single $1.35\ M_\odot$ TOV star described by DD2. The mesh-generating point setup in the isolated star simulation is identical to the one which we employ for each individual star in the binary, while we keep the same metric resolution, atmosphere parameters and refinement/derefinement criteria. Discretization errors by the finite resolution excite oscillations in the maximum density and the minimum lapse function. Comparing the calculations of the isolated star and the binary, the frequencies are similar, while the amplitudes are slightly higher in the case of the isolated neutron star. Hence, we conclude that the setup of our binary initial data works robustly and that the procedure does not introduce additional errors apart from those which are expected, i.e. truncation errors.

5.2 Simulations

5.2.1 General dynamics

Figure 3 shows the evolution of the maximum rest-mass density $\rho_{\rm max}$ during the simulation. The vertical dashed line indicates the time

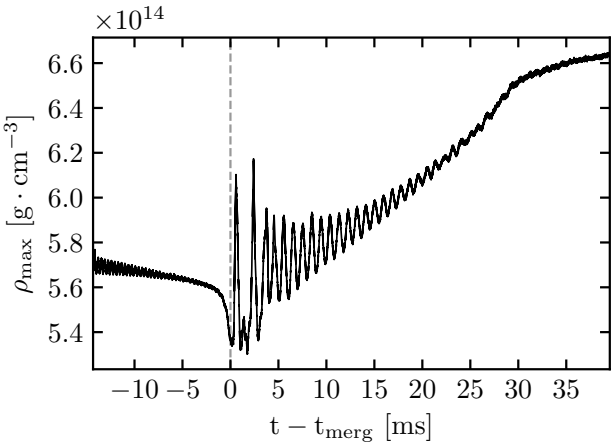

Figure 3. Maximum rest-mass density as a function of time for a BNS system with two $1.35\ M_\odot$ neutron stars modelled with the DD2 EOS. The vertical dashed line indicates the time of merging.

when the two neutron stars merge $t_{\rm merg}$[3] and separates the inspiral and the post-merger phase. The main stages of the binary evolution are shown in Fig. 4, where we present the rest-mass density in the orbital plane of the binary at four different times. The top left and top right panels correspond to snapshots taken during the inspiral and right after merging, respectively. Middle and bottom row panels present two times at the late stages of the post-merger evolution on a logarithmic and on a linear scale. We evolve the binary for ≈ 39.5 ms after the stars merge.

Throughout the inspiral the two neutron stars revolve around each other, while the orbital separation decreases due to energy and angular momentum losses by GWs. As mentioned, during the inspiral the maximum density features small oscillations (Fig. 3) because discretization errors excite dominantly the radial mode. As the binary components approach each other, tidal effects become more pronounced. The tidal deformations are visible in the top left panel of Fig. 4, which corresponds to the last few revolutions before the stars merge.

The stars collide with a relatively large impact parameter. The collision results in the sudden increase of the maximum density immediately after $t_{\rm merg}$ in Fig. 3 and shock-heating of material at the collision interface. Figure 5 shows snapshots of the temperature[4] T in the orbital plane right after merging (top row), when the system reaches the highest temperatures, as well as two snapshots in the post-merger phase (bottom row). As shown in the upper panels of Fig. 5, matter at the collision interface of the two neutrons stars reaches temperatures of almost 90 MeV. In Fig. 5 we also overplot contour lines corresponding to two different densities. The white dashed line indicates where the density equals $10^{13}\ {\rm g \cdot cm^{-3}}$ to highlight the region containing the bulk of matter at the times shown in the plots. The solid white line corresponds to a density of $2.7 \times 10^{14}\ {\rm g \cdot cm^{-3}}$ (nuclear saturation density). Most of the high-density parts of the stars, except for matter at the collision interface, remain cold even during the merger phase. The highest temperatures are reached in hotspots

[3] We define $t_{\rm merg}$ as the time when the GW signal amplitude reaches its maximum.

[4] We estimate the temperature based on the thermal energy through $\epsilon_{\rm th} = \frac{kT}{m_{\rm B}(\Gamma_{\rm th}-1)}$, where k is the Boltzmann constant and m_B the baryon mass.

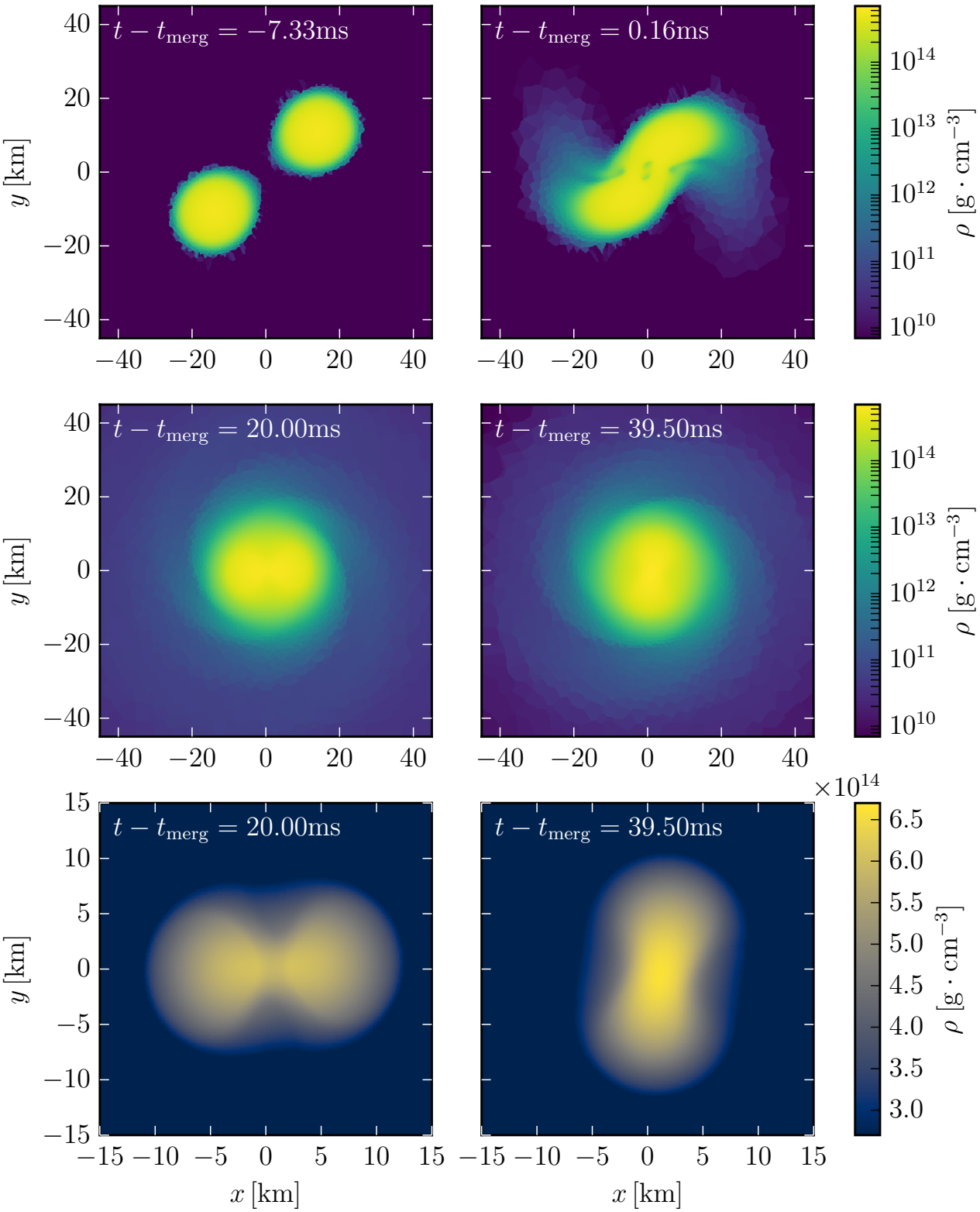

Figure 4. Evolution of the rest-mass density for the BNS merger simulation. Each panel shows a slice through the orbital plane of the binary. The densities in the upper and middle rows are displayed on a logarithmic scale, while the bottom row focuses on the high-density material of the remnant employing a linear density scale. The times are chosen such that the top row panels show snapshots from the inspiral stage and the moment of merging, while the middle row panels display very late stages of the post-merger evolution. The times in the bottom row panels match those in the middle row.

with densities slightly below 2.7×10^{14} g $\cdot$ cm^{-3}. The densities are lower in these blobs because of the significant thermal pressure at these temperatures. These regions are also visible in the top right panel of Fig. 4 and form due to the mixing of material from the two stars (see e.g. Kastaun et al. 2016). The contact interface between the two stars is subject to the Kelvin-Helmholtz instability. The distribution and evolution of the temperature in the upper row of Fig. 5 is indicative of the local vorticity (see e.g. Kiuchi et al. 2015).

In the post-merger phase, a double-core structure forms. We observe that our simulation preserves the double-core structure for more than 20 ms after $t_{\rm merg}$. This is clearly shown in the middle and bottom rows of Fig. 4, as well as the bottom row of Fig. 5. The two cores (enclosed in the white solid contour line in the bottom left panel of Fig. 5) can be clearly identified 20 ms after merging. The centers of the cores merge at $t - t_{\rm merg} \approx 28$ ms. Even at the very late stages of the evolution, i.e. at $t - t_{\rm merg} = 39.5$ ms, the high-density material has not yet settled to a single spherically-shaped core, but exhibits a bar-shaped structure. The double-core phase in our simulation lasts significantly longer compared to other simulations with fixed-grid finite-volume approaches (see e.g. Kastaun et al. 2016; Hanauske et al. 2017). Similarly, the quasi-radial mode survives for a long time after merging as shown in Fig. 3.

The cores remain cold during the whole post-merger evolution. The remnant still exhibits high temperatures, up to ≈ 40 MeV. These highest temperatures at late times occur at the outer edges of the shearing interface between the two cold cores. The system exhibits density spiral arms starting at the central object during the whole post-merger phase that we simulate, as can be seen in both middle row panels of Fig. 4 and in the bottom row panels of Fig. 5.

By eye, one cannot identify the development of a pronounced $m = 1$ instability in the evolution of the rest-mass density in the orbital plane until the end of the simulation (Paschalidis et al. 2015; Lehner et al. 2016; East et al. 2016; Radice et al. 2016a). For comparison, we simulate the binary system with an SPH code, which also adopts the conformal flatness approximation (Oechslin et al. 2002, 2007). We employ the same EOS treatment and choose a resolution of roughly 3×10^5 SPH particles in total[5]. In the SPH simulation the $m = 1$ instability does clearly occur for the same binary system.

We briefly examine the angular velocity profile[6] in the equatorial plane at different stages of the post-merger evolution in Fig. 6. The rotation profile initially exhibits a maximum at the center of the remnant. The value of the time- and azimuthially-averaged angular velocity Ω at the center decreases over time and at later times an off-center peak forms. The off-center maximum first appears at $t - t_{\rm merg} \approx 28$ ms at a radial distance of ≈ 4 km. Over time the position of the peak moves outwards from the center to about ≈ 7 km at the end of the simulation. The qualitative characteristics of the angular velocity profile agree with what is reported in other simulations (see e.g. Shibata et al. 2005; Kastaun et al. 2016; Hanauske et al. 2017; Guilet et al. 2017), but the evolution of the profile and the overall angular momentum redistribution happens over longer timescales. A similar delay in the evolution of the Ω profile has been reported in Kiuchi et al. (2018) for simulations with very high resolution. The latter calculations, however, employ a different EOS and include magnetic fields, which is why a direct comparison is difficult.

Overall, the general dynamics and the qualitative features of our simulation are consistent with what is found in other simulations. A notable difference is that the double-core structure and the quasi-radial oscillations persist for a longer time. Similarly, an off-center peak of the angular velocity profile emerges only at relatively late times. These points hint that the evolution with the moving-mesh setup has low numerical viscosity (see also the discussion on the damping of the GW signal in Sec. 5.2.2).

Finally, we comment on the resolution of our simulation. In principle, we cannot define a single resolution in moving-mesh simulations, because cells do not have a fixed shape and volume. This is clearly visible in both Figs. 4 and 5, where in lower density regions the cell shapes are visible. We can however estimate the resolution under some assumption for the cell geometry. Here we assume that cells are spheres and focus on the high-density regions. For material with $\rho > 0.5 \times \rho_{\rm max}$ at a given time we compute the average cell volume and in turn the cell radius. We then estimate the mean distance between cell centers in these regions as twice the computed radius. Throughout the post-merger phase, we obtain an average distance between cell centers of approximately $0.11\ M_\odot \approx 162$ m in regions with rest-mass density above 50% of $\rho_{\rm max}$. Naturally, some cells are smaller (or larger) than what this number indicates. This highlights the ability of our implementation to reach resolutions which are roughly comparable to what is currently used in merger simulations, although typically with high-order schemes. Our simulation required a few weeks of computing time running on 192 cores. In the future we plan to perform simulations with even higher resolution.

5.2.2 *Gravitational wave signal*

In Fig. 7 we show the plus polarization of the GW signal[7] assuming a distance of 40 Mpc along the polar axis. The vertical dashed line in Fig. 7 indicates the merging time. Before $t_{\rm merg}$ the system emits GWs with a frequency twice as large as the orbital frequency. As the stars approach each other, the frequency, as well as the amplitude of the GW signal, increase. The coalescence of the stars excites a number of modes in the post-merger remnant, which shape the post-merger GW signal.

Notably, the damping of the post-merger GW signal is very slow for the approximately 39.5 ms of post-merger evolution, which is in agreement with our observation in Sec. 5.2.1 that numerical viscosity is relatively low in this simulation. We determine the damping time to be $\tau_{\rm peak} \approx 48$ ms based on the analytic model presented by Soultanis et al. (2022). The SPH simulation yields $\tau_{\rm peak} \approx 10.5$ ms. Soultanis et al. (2022) perform fully general relativistic simulations with a fixed grid and obtain $\tau_{\rm peak} < 11$ ms for all their models and resolutions ($\tau_{\rm peak} \approx 7$ ms for the binary system with total gravitational mass of $2.7\ M_\odot$), which is significantly below our current result. We do however note that Soultanis et al. (2022) employ a different EOS, which does not allow for a direct comparison with our simulation.

In Fig. 8 we present the Fourier transform of the h_+ polarization as measured at 40 Mpc. The solid line corresponds to the spectrum of the full GW signal from the whole evolution, while the dotted line is the Fourier transform of the signal from the post-merger phase

[5] The SPH particle number as measure of the resolution should not be directly compared to the number of resolving elements in a grid code. Effectively, the resolution of the SPH run is lower compared to the moving-mesh simulation.

[6] We define the angular velocity as $\frac{xv^y - yv^x}{\sqrt{x^2+y^2}}$ where $v^i = u^i/u^0$. All quantities are computed with respect to the center of mass of matter with $\rho > 0.95 \times \rho_{\rm max}$ and we consider time- and azimuthially-averaged profiles.

[7] We conservatively multiply the signal by a factor 1.4 to account for the underestimation of the amplitude by the quadrupole formula (Shibata et al. 2005, likely the factor is closer to 2 comparing recent simulations (Soultanis et al. 2022)).

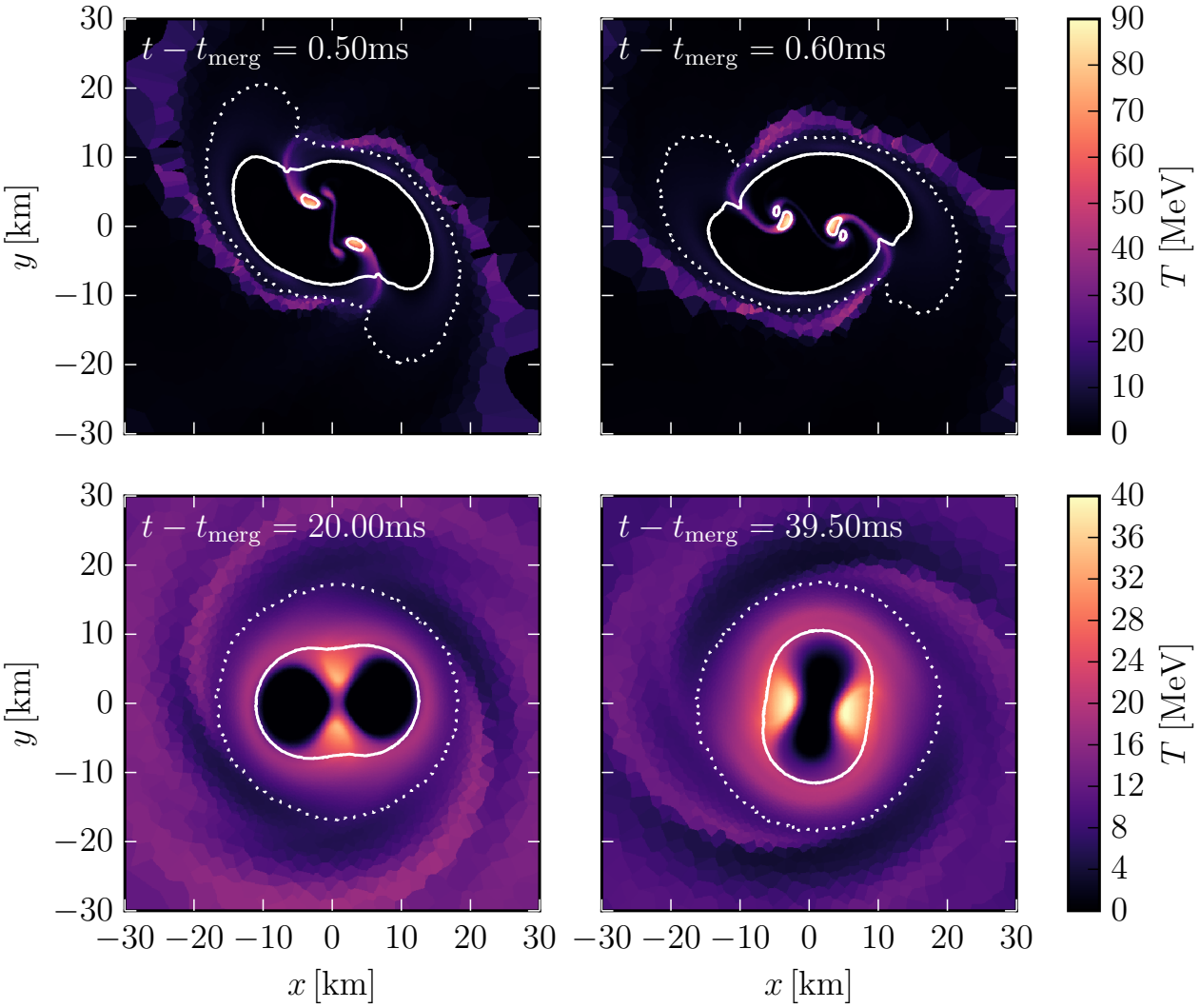

Figure 5. Temperature in the orbital plane for the BNS merger simulation. The top row shows snapshots right after the neutron stars merge, when the temperature reaches the highest value of $T \approx 90$ MeV. The bottom row presents snapshots taken at 20 ms and 39.5 ms after merging. White dotted and solid contours indicate densities of 10^{13} g $\cdot$ cm^{-3} and 2.7×10^{14} g $\cdot$ cm^{-3}, respectively. The two cold, high-density cores are clearly visible at late stages of the evolution (bottom panels).

alone. In addition, we show the design sensitivity of Advanced LIGO (LIGO Scientific Collaboration et al. 2015) and the Einstein Telescope (Punturo et al. 2010) with the upper and lower dash-dotted lines, respectively. We extract the main oscillation frequency in the spectrum (marked by a vertical dashed line) at $f_{\rm peak} = 2.56$ kHz. For comparison, in our SPH simulation of the same binary system (see Sec. 5.2.1) we obtain $f_{\rm peak} = 2.62$ kHz, which is in good agreement with our current result. In comparison to the SPH simulation, the features in the GW spectrum in Fig. 8 are more pronounced likely due to the low numerical damping of the signal. In addition, we compare to fully general relativistic simulations of the binary system from the CORE database[8] (Dietrich et al. 2018). We extract $f_{\rm peak} = 2.57$ kHz and $f_{\rm peak} = 2.65$ kHz for the two available simulations with finest grid resolutions of 0.125 $M_\odot$ and 0.083 $M_\odot$ respectively (see Radice et al. 2016b, 2017, for more details). Both frequencies agree rather well with our result noting that these static-mesh simulations employed the full temperature-dependent EOS table.

The spectrum in Fig. 8 contains several subdominant features, which are in principle observable. In particular there is a pronounced broad peak at about 1.8 kHz. This peak emerges from the rotation of two antipodal tidal bulges, which form right after the merging. These tails rotate at a slower rate than the high-density parts and produce a peak at a frequency $f_{\rm spiral}$ (Bauswein & Stergioulas 2015). In this particular simulation we obtain $f_{\rm spiral} = 1.79$ kHz, roughly 200 Hz lower than in the SPH simulation. The amplitude of the peak in the moving-mesh simulation is in comparison to the SPH calculation increased. Since the gravity solver is identical in both simulations, the different properties of this secondary peak hint to some sensitivity of this feature to the hydrodynamics scheme.

In Fig. 8 we also indicate the frequencies $f_{2\pm0}$ originating from the non-linear coupling between the dominant oscillation mode $f_{\rm peak}$

[8] http://www.computational-relativity.org

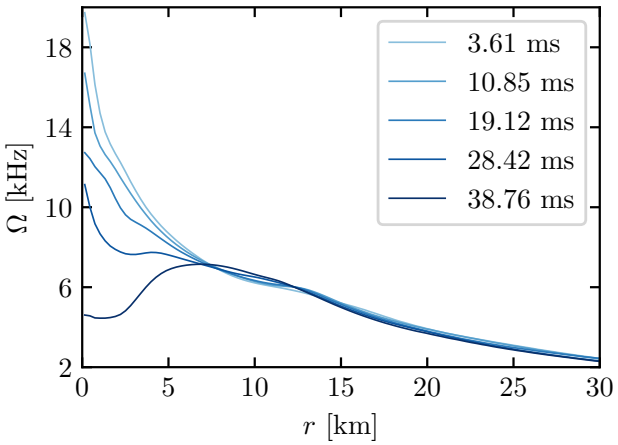

Figure 6. Rotation profile of the remnant at different times after merging. The angular velocity Ω is averaged along the azimuthial direction and over a time interval of 1 ms. The legend indicates $t - t_{\rm merg}$ for each line, where t refers to the midpoint of the respective 1 ms time interval.

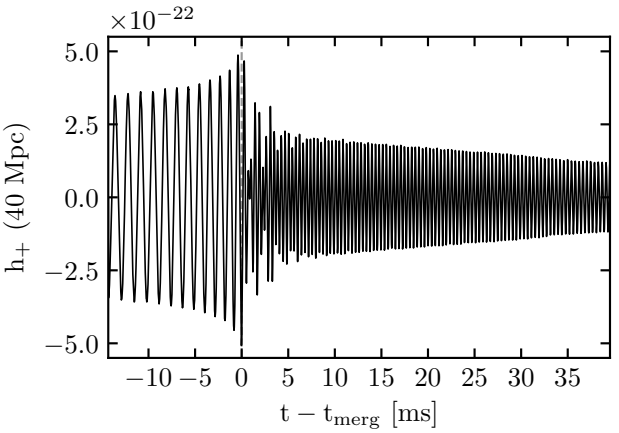

Figure 7. Gravitational wave amplitude of the plus polarization at a distance of 40 Mpc for the BNS simulation. The vertical dashed line shows the merging time.

and the quasi-radial oscillation mode f_0 (Stergioulas et al. 2011). To identify this feature, we estimate f_0 from the evolution of the lapse function and tag the peaks which occur at $\approx f_{\rm peak} \pm f_0$ in the GW spectrum.

6 SUMMARY

In this work we extend the (originally Newtonian) moving-mesh Arepo code to general relativistic hydrodynamics employing the flux-conservative Valencia formulation. We couple the implementation with a solver of the Einstein field equations imposing the conformal flatness approximation. This new tool can in principle be applied to a variety of astrophysical scenarios including those that require the dynamical evolution of the spacetime. In this work we focus on applications to neutron stars and neutron star mergers and supplement the code with a module to include a high-density EOS.

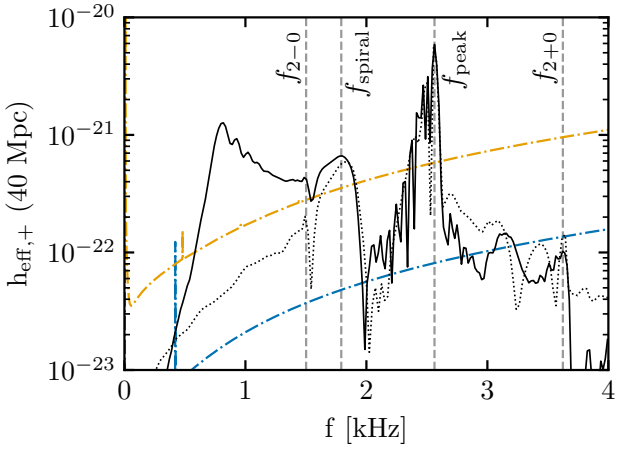

Figure 8. Gravitational wave spectrum of the plus polarization at a distance of 40 Mpc. The solid line refers to the whole simulation, while the dotted line displays the spectrum of only the post-merger phase. The vertical dashed lines indicate the frequency peaks $f_{\rm peak}$, $f_{\rm spiral}$, f_{2-0} and f_{2+0}. The upper (orange) and lower (blue) dash-dotted lines denote the design sensitivity of Advanced LIGO (LIGO Scientific Collaboration et al. 2015) and the Einstein Telescope (Punturo et al. 2010), respectively.

We validate the implementation by performing different test calculations, which can be compared to independent results. We simulate isolated, static neutron stars with a fixed spacetime (Cowling approximation) and with a dynamical spacetime (TOV tests). In both tests the code preserves very well the density profile of the initial equilibrium model. The frequencies of radial oscillations, which are excited by truncation errors and an added perturbation, coincide very well with perturbative results and simulations from other codes, which verifies our implementation. We run simulations with moving meshes and static meshes which allow a more direct comparison to existing calculations. Arepo offers the advantage that the initial grid configuration can be freely chosen and adapted to the specific problem to be simulated. We employ different choices including a Cartesian mesh and a spherical distribution of the mesh-generating points. The implementation presented here represents the first general relativistic moving-mesh code with a dynamical spacetime evolution.

We present the first moving-mesh simulation of a neutron star merger including the inspiral phase and the post-merger evolution, which we run until roughly 40 milliseconds after merging. The initial mesh setup approximately follows the mass distribution and geometry of the system. For the merger calculation we employ an additional feature of Arepo, namely the adaptive refinement and derefinement of computational cells during the simulation. We find that in the high-density regime criteria to approximately achieve a target mass of the grid cells, which is comparable to the initial setup, work well in merger simulations. Although one cannot define a unique resolution in moving-mesh simulations, the typical cell size in the high-density merger remnant is roughly 150 meters in our simulation. The computational costs for this setup are modest (a few weeks on about 200 cores) and thus even higher resolutions are well achievable. The choice of the initial mesh setup and the refinement/derefinement criteria introduce a certain flexibility, which we will explore in future work with the prospect of further increasing the performance of the tool in merger simulations and possibly identifying choices well-adapted to specific problems or questions in this context.

We analyze the dynamics and the gravitational wave emission of

the moving-mesh merger simulation. We find a general agreement with other simulations based on either SPH or static-mesh schemes. In comparison, our moving-mesh calculation seems to preserve the structure of the early post-merger remnant for a longer time. The initial double-core structure persists for more than 20 milliseconds after merging. The quasi-radial oscillation of the remnant is only slowly damped and the profile of the angular velocity evolves on longer time scales. This behavior may prolongate the life time of the remnant although we do not run this specific simulation until the gravitational collapse takes place. Notably, the amplitude of the post-merger gravitational wave emission decreases only slowly and is still large even at the end of the simulation at roughly 40 milliseconds after merging. These characteristics point to a very low numerical viscosity. The frequency of the dominant post-merger oscillation is in good agreement with results from simulations employing other hydrodynamics schemes. At any rate these first results are very encouraging and show that the moving-mesh approach can be very beneficial for the simulation of BNS mergers.

The work presented in this paper will be the basis for more extensive studies and further developments with the new general relativistic moving-mesh code. The inclusion of fully temperature- and composition-dependent EOS tables and neutrino transport is in progress. Other more technical aspects to be addressed in the future concern the Riemann solver, choices for the grid setup, cell merging and splitting, and the atmosphere treatment. The original Arepo code already includes magnetic fields, which may be extended to the relativistic implementation. The currently employed conformal flatness approximation may be replaced by a full solver noting that the infrastructure for communication between the unstructured hydrodynamics grid and overlaid Cartesian grids is already available. The general flexibility and adaptivity of Arepo suggest to employ the relativistic version for other relativistic astrophysical scenarios, e.g. black hole accretion discs and neutron star-black hole mergers.

ACKNOWLEDGEMENTS

We thank S. Blacker, E. Müller, S. Ohlmann and N. Stergioulas for helpful discussions. G.L. and A.B. acknowledge support by the European Research Council (ERC) under the European Union's Horizon 2020 research and innovation programme under grant agreement No. 759253. A.B. and F.K.R. acknowledge support by Deutsche Forschungsgemeinschaft (DFG, German Research Foundation) - Project-ID 138713538 - SFB 881 ("The Milky Way System", subproject A10). A.B. acknowledges support by DFG - Project-ID 279384907 - SFB 1245 and support by the State of Hesse within the Cluster Project ELEMENTS. T.S. is Fellow of the International Max Planck Research School for Astronomy and Cosmic Physics at the University of Heidelberg (IMPRS-HD) and acknowledges financial support from IMPRS-HD. The work of T.S. and F.K.R. is supported by the Klaus Tschira Foundation. The simulations of this paper were performed on the Virgo cluster at GSI Helmholtzzentrum für Schwerionenforschung, Darmstadt.

DATA AVAILABILITY

The data underlying this article will be shared on reasonable request to the corresponding author.

REFERENCES

Abbott B. P., et al., 2017a, Phys. Rev. Lett., 119, 161101
Abbott B. P., et al., 2017b, ApJ, 848, L12
Abbott B. P., et al., 2019, Physical Review X, 9, 011001
Alcubierre M., 2008, Introduction to 3+1 Numerical Relativity. International Series of Monographs on Physics, OUP Oxford
Antoniadis J., et al., 2013, Science, 340, 448
Arnowitt R., Deser S., Misner C. W., 2008, Gen. Relativ. Gravit, 40, 1997
Arzoumanian Z., et al., 2018, Astrophys. J., Suppl. Ser., 235, 37
Ayache E. H., van Eerten H. J., Eardley R. W., 2022, MNRAS, 510, 1315
Baiotti L., Rezzolla L., 2017, Reports on Progress in Physics, 80, 096901
Banyuls F., Font J. A., Ibáñez J. M., Martí J. M., Miralles J. A., 1997, ApJ, 476, 221
Baumgarte T. W., Shapiro S. L., 2010, Numerical Relativity: Solving Einstein's Equations on the Computer. Cambridge University Press, doi:10.1017/CBO9781139193344
Baumgarte T. W., Cook G. B., Scheel M. A., Shapiro S. L., Teukolsky S. A., 1998, Phys. Rev. D, 57, 7299
Bauswein A., Stergioulas N., 2015, Phys. Rev. D, 91, 124056
Bauswein A., Janka H. T., Oechslin R., 2010, Phys. Rev. D, 82, 084043
Bauswein A., Janka H. T., Hebeler K., Schwenk A., 2012, Phys. Rev. D, 86, 063001
Bauswein A., Goriely S., Janka H. T., 2013, ApJ, 773, 78
Bauswein A., Blacker S., Lioutas G., Soultanis T., Vijayan V., Stergioulas N., 2021, Phys. Rev. D, 103, 123004
Blanchet L., Damour T., Schaefer G., 1990, MNRAS, 242, 289
Briggs W. L., Henson V. E., McCormick S. F., 2000, A Multigrid Tutorial (2nd Ed.). Society for Industrial and Applied Mathematics, USA
Chang P., Etienne Z. B., 2020, MNRAS, 496, 206
Chang P., Wadsley J., Quinn T. R., 2017, MNRAS, 471, 3577
Cromartie H. T., et al., 2020, Nature Astronomy, 4, 72
Darwish M., Moukalled F., 2003, International Journal of Heat and Mass Transfer, 46, 599
Demorest P. B., Pennucci T., Ransom S. M., Roberts M. S. E., Hessels J. W. T., 2010, Nature, 467, 1081
Dietrich T., et al., 2018, Classical and Quantum Gravity, 35, 24LT01
Dimmelmeier H., Stergioulas N., Font J. A., 2006, MNRAS, 368, 1609
Duffell P. C., MacFadyen A. I., 2011, ApJS, 197, 15
Duffell P. C., MacFadyen A. I., 2012, ApJ, 755, 7
Duffell P. C., MacFadyen A. I., 2013, ApJ, 775, 87
Dumbser M., Boscheri W., Semplice M., Russo G., 2017, SIAM J. Sci. Comput., 39
East W. E., Paschalidis V., Pretorius F., Shapiro S. L., 2016, Phys. Rev. D, 93, 024011
Einfeldt B., 1988, SIAM Journal on Numerical Analysis, 25, 294
Faber J. A., Rasio F. A., 2012, Living Reviews in Relativity, 15, 8
Faye G., Schäfer G., 2003, Phys. Rev. D, 68, 084001
Font J. A., 2008, Living Reviews in Relativity, 11, 7
Font J. A., et al., 2002, Phys. Rev. D, 65, 084024
Foucart F., Laguna P., Lovelace G., Radice D., Witek H., 2022, arXiv e-prints, p. arXiv:2203.08139
Gaburov E., Johansen A., Levin Y., 2012, ApJ, 758, 103
Gaburro E., Boscheri W., Chiocchetti S., Klingenberg C., Springel V., Dumbser M., 2020, Journal of Computational Physics, 407, 109167
Gondek D., Haensel P., Zdunik J. L., 1997, A&A, 325, 217
Górski K. M., Hivon E., Banday A. J., Wandelt B. D., Hansen F. K., Reinecke M., Bartelmann M., 2005, ApJ, 622, 759
Gourgoulhon E., Grandclément P., Taniguchi K., Marck J.-A., Bonazzola S., 2001, Phys. Rev. D, 63, 064029
Gronow S., Collins C. E., Sim S. A., Röpke F. K., 2021, A&A, 649, A155
Guilet J., Bauswein A., Just O., Janka H.-T., 2017, MNRAS, 471, 1879
Hanauske M., Takami K., Bovard L., Rezzolla L., Font J. A., Galeazzi F., Stöcker H., 2017, Phys. Rev. D, 96, 043004
Harten A., 1983, J. Comput. Phys., 49, 357
Harten A., 1984, SIAM Journal on Numerical Analysis, 21, 1
Harten A., Lax P. D., Leer B. V., 1983, SIAM Review, 25, 35
Hempel M., Schaffner-Bielich J., 2010, Nucl. Phys. A, 837, 210

Isenberg J., Nester J., 1980, in General Relativity and Gravitation. Vol. 1. One hundred years after the birth of Albert Einstein. Edited by A. Held. New York. p. 23
Janka H.-T., 2012, Annual Review of Nuclear and Particle Science, 62, 407
Janka H. T., Zwerger T., Moenchmeyer R., 1993, A&A, 268, 360
Kastaun W., Ciolfi R., Giacomazzo B., 2016, Phys. Rev. D, 94, 044060
Kiuchi K., Cerdá-Durán P., Kyutoku K., Sekiguchi Y., Shibata M., 2015, Phys. Rev. D, 92, 124034
Kiuchi K., Kyutoku K., Sekiguchi Y., Shibata M., 2018, Phys. Rev. D, 97, 124039
Kölsch M., Dietrich T., Ujevic M., Bruegmann B., 2021, arXiv e-prints, p. arXiv:2112.11851
Koudmani S., Sijacki D., Bourne M. A., Smith M. C., 2019, MNRAS, 484, 2047
LIGO Scientific Collaboration et al., 2015, Classical and Quantum Gravity, 32, 074001
Lackey B. D., Nayyar M., Owen B. J., 2006, Phys. Rev. D, 73, 024021
Lehner L., Liebling S. L., Palenzuela C., Motl P. M., 2016, Phys. Rev. D, 94, 043003
Linares M., Shahbaz T., Casares J., 2018, Astrophys. J, 859, 54
Liptai D., Price D. J., 2019, MNRAS, 485, 819
Martí J. M., Müller E., 2015, Living Reviews in Computational Astrophysics, 1, 3
Oechslin R., Rosswog S., Thielemann F.-K., 2002, Phys. Rev. D, 65, 103005
Oechslin R., Janka H. T., Marek A., 2007, Astron. Astrophys., 467, 395
Ohlmann S. T., Röpke F. K., Pakmor R., Springel V., 2016, ApJ, 816, L9
Ohlmann S. T., Röpke F. K., Pakmor R., Springel V., 2017, A&A, 599, A5
Pakmor R., Kromer M., Taubenberger S., Springel V., 2013, ApJ, 770, L8
Pakmor R., Springel V., Bauer A., Mocz P., Munoz D. J., Ohlmann S. T., Schaal K., Zhu C., 2016, MNRAS, 455, 1134
Pakmor R., et al., 2022, arXiv e-prints, p. arXiv:2203.14990
Paschalidis V., East W. E., Pretorius F., Shapiro S. L., 2015, Phys. Rev. D, 92, 121502
Punturo M., et al., 2010, Classical and Quantum Gravity, 27, 194002
Radice D., Bernuzzi S., Ott C. D., 2016a, Phys. Rev. D, 94, 064011
Radice D., Galeazzi F., Lippuner J., Roberts L. F., Ott C. D., Rezzolla L., 2016b, MNRAS, 460, 3255
Radice D., Bernuzzi S., Del Pozzo W., Roberts L. F., Ott C. D., 2017, ApJ, 842, L10
Read J. S., Lackey B. D., Owen B. J., Friedman J. L., 2009, Phys. Rev. D, 79, 124032
Rezzolla L., Zanotti O., 2013, Relativistic Hydrodynamics. OUP Oxford
Rosswog S., 2015, Living Reviews in Computational Astrophysics, 1, 1
Rosswog S., Diener P., 2021, Classical and Quantum Gravity, 38, 115002
Ryan G., MacFadyen A., 2017, ApJ, 835, 199
Schneider F. R. N., Ohlmann S. T., Podsiadlowski P., Röpke F. K., Balbus S. A., Pakmor R., Springel V., 2019, Nature, 574, 211
Shibata M., 2015, Numerical Relativity. 100 years of general relativity, World Scientific Publishing Company Pte Limited
Shibata M., Taniguchi K., Uryū K., 2005, Phys. Rev. D, 71, 084021
Soultanis T., Bauswein A., Stergioulas N., 2022, Phys. Rev. D, 105, 043020
Springel V., 2010, MNRAS, 401, 791
Stergioulas N., Bauswein A., Zagkouris K., Janka H.-T., 2011, MNRAS, 418, 427
Typel S., Röpke G., Klähn T., Blaschke D., Wolter H. H., 2010, Phys. Rev. C, 81, 015803
Vandenbroucke B., De Rijcke S., 2016, Astronomy and Computing, 16, 109
Villar V. A., et al., 2017, ApJ, 851, L21
Vogelsberger M., Sijacki D., Kereš D., Springel V., Hernquist L., 2012, MNRAS, 425, 3024
Vogelsberger M., et al., 2014, Nature, 509, 177
Weinberger R., Ehlert K., Pfrommer C., Pakmor R., Springel V., 2017, MNRAS, 470, 4530
Weinberger R., Springel V., Pakmor R., 2020, ApJS, 248, 32
Wilson J. R., Mathews G. J., 2003, Relativistic Numerical Hydrodynamics. Cambridge Monographs on Mathematical Physics, Cambridge University Press, doi:10.1017/CBO9780511615917
Wilson J. R., Mathews G. J., Marronetti P., 1996, Phys. Rev. D, 54, 1317
Yalinewich A., Steinberg E., Sari R., 2015, ApJS, 216, 35
van Leer B., 1977, Journal of Computational Physics, 23, 276

This paper has been typeset from a TEX/LATEX file prepared by the author.